Original Article

Development and characterisation of novel three-dimensional axisymmetric chiral auxetic structures

Nejc Novak [a,], Anja Mauko [a], Miran Ulbin [a], Lovre Krstulović-Opara [b], Zoran Ren [a], Matej Vesenjak [a]*

[a] Faculty of Mechanical Engineering, University of Maribor, Maribor, Slovenia
[b] Faculty of Electrical Engineering, Mechanical Engineering and Naval Architecture, University of Split, Split, Croatia

ARTICLE INFO

ABSTRACT

Novel three-dimensional (3D) axisymmetric chiral structures with negative and zero Poisson's ratios are presented based on the existing 3D conventional chiral unit cell. The conventional tetra-chiral unit cell is mapped to the axisymmetric space to form the new 3D axisymmetric chiral structure. Two different structure designs are characterised depending on the period delay of the sine curve representing the horizontal struts of the structure. The structures are fabricated using additive manufacturing technology and experimentally tested under compression loading conditions. The digital image correlation methodology is used to determine the Poisson's ratio dependence on the axial strain. The computational model of axisymmetric chiral structures is developed and validated using the experimental data. The computational model is then used to evaluate the new virtual axisymmetric chiral structures with graded cell structures. The newly developed axisymmetric structures show enhanced mechanical properties when compared to the existing 3D chiral structures.

1. Introduction

The auxetic cellular structures are novel cellular meta-materials with a negative Poisson's ratio, which are very useful in various fields of engineering, medicine, sport and fashion due to their unique deformation behaviour [1,2]. Such structures shrink in transversal direction while being compressed and vice versa in the case of tensile loading. Their development started more than 30 years ago, and many, primarily 2D and orthogonal 3D geometries have been developed and analysed since then. The auxetic deformation behaviour can be achieved on nano, micro or macro level since the underlying kinematic deformation system is scalable. The currently known auxetic structures have predominantly orthotropic properties, e.g. 2D honeycombs [3,4], 3D structures [5,6], composites [7], while the truly three-dimensional isotropic structures have yet to be developed.

The tubular or/and axisymmetric structures and structures with similar circular hollow cross-sections with mainly radially

graded density can be found in nature [8,9]. These building approaches of nature were also adopted in many engineering applications and are among the most used structures in engineering. Such mimicking structures are, for example, crash tubes [10,11], crash boxes [12], also with axially graded porosity which results in multi-stage behaviour [13] and tubular joints [14,15]. These studies report on the excellent mechanical properties of hollow circular tubes compared to their solid counterparts, especially of energy absorption capacity during an axial impact. The drawbacks of these structures represent progressive buckling and unstable deformation pattern in engineering applications, while in the case of medical stents, the crushing and removal still present some significant challenges. These drawbacks can be minimised or limited with individualised tailoring (programming) of the Poisson's ratio of cylindrical structures as it was demonstrated in [16,17], or using different cellular structures for the tube body [18].

The auxetic tubular structures are mostly limited to different two-dimensional auxetic geometry mapped on the surface of the tube [19]. The re-entrant unit cells were mapped on the tube's surface and studied using the finite element simulations in [20]. The rotating rigid units were also considered for the auxetic tubular structure [21], as well as auxetic chiral unit cells [22—24], perforated sheets [25,26], and W geometry [27]. At that point, it should be noted that by extending the auxetic 2D geometry in the radial direction, the extension should be relatively limited to retain the auxetic effect and prevent progressive and non-controlled buckling. Therefore, the three-dimensional unit cells were also used for the tubular structures, like 3D re-entrant cells [28], where the authors showed that the auxetic cellular tubes have a better response under compressive loading compared to equivalent solid tubes. One way to overcome the problem with buckling is to form the 3D structure by mapping the 2D auxetic geometry to the circumferential direction and not to radial as it was done in most previously presented cases. This was done with chiral, re-entrant and star-shaped geometries in [29].

The tubular structures with fillers achieve superior properties under different loading conditions, as shown in [30]. Most of the voids of the presented auxetic structures are not filled, while with foam-filled auxetic structures, the energy absorption capacity can be superior to hollow ones. This was shown in the case of W geometry [31]. The same effect as in the foam-filled tube can also be achieved with the density graded cellular structure, in the same way as observed in nature (e.g. varying bone density in a radial direction).

In this work, the newly developed fully 3D axisymmetric chiral auxetic structure is presented, fabricated and then experimentally and computationally evaluated. The structure is based on the regular 3D chiral unit cells mapped to the 3D axisymmetric space to form the 3D chiral axisymmetric structure.

2. Specimen geometry

The axisymmetric chiral cellular structure (ACS) with a cylindrical shape presented in this work is built from the unit chiral cells with their shape corresponding to the 10th eigenmode of the regular cubic unit cell, which was presented in [32], and studied in detail in [33—35]. The geometry of the presented axisymmetric chiral cellular structure is pending the patent at the European patent office [36]. The regular, non-axisymmetric geometry of the chiral structure was already studied in our previous work [37—39]. The three-dimensional chiral unit cell represents a lattice structure composed of curved struts joined at cube vertices (nodes), thus forming an open-cellular structure with very low structural weight. The struts take the shape of sines, whose turning points meet in the nodes and can have concave or convex curvature depending on their spatial orientation. The structure exhibits auxetic deformation behavior upon mechanical loading with negative Poisson's ratio in polar (axisymmetric structure) or spherical (spherical structure) directions.

Several possible embodiments of the axisymmetric chiral auxetic structure are possible, with regards to the i) base material, which is metal or non-metal, ii) struts of unit cells, which can differ in cross-section shape, i.e., circular, triangular, quadrilateral; thickness; length; curvature, e.g., polynomial, trigonometric; the connection of adjoining or opposite nodes, iii) unit cells, which can differ in size and closure of the cell windows (i.e., closed or open cells), iv) distribution of unit cells in space.

The above-listed parameters may be uniform throughout the cellular structure or vary in the axial, radial, or circumferential direction. The latter leads to graded axisymmetric chiral auxetic structures with spatially variable properties. The graded structures offer the detailed adoption of the geometry and its mechanical and deformation behavior to the estimated loading scenarios.

The unit cell geometry is shown in Fig. 1f, where the geometrical parameters l, h and A are determined. The height of the unit cell h and amplitude A in horizontal struts are kept constant in the sample, while amplitude A in vertical struts and length of unit cell l are changing in the radial direction. The original axisymmetric chiral structure (ACS_v1) presented in this work (Fig. 1a) was built from the unit chiral cell that was first scaled and copied in the radial direction starting from the outermost layer towards the structure axis (direction r) to form a single radial slice layer. The slice layer was then repeatedly copied along the axis (direction h) to form a radial slice as a part of the axisymmetric arrangement. This slice was then copied repeatedly in the circumferential direction around the structure axis (direction φ) to form the final axisymmetric structure. The corresponding axisymmetric chiral structure generator was developed for that purpose in Ansys Spaceclaim software using the Python script (Ansys® Academic Research Mechanical, Release 2021 R2). The generator allows for different scale factors for radial and vertical transformation to build the ACS with spatially graded cellular structure with varying strut thickness, unit cell size, and the unit cells' amplitude.

The second ACS structure (ACS_v2) was also developed and analysed in this study, where the horizontal struts have the same sine shapes as in the case of ACS_v1, but without half period delay in every second horizontal layer of the structure, i.e., the maximum and minimum of the sine curve are at the same circumferential position in each layer.

One ACS_v1 and two ACS_v2 structures with different relative densities and dimensions ⌀20 mm × 20 mm were generated for this study. The geometrical parameters of the
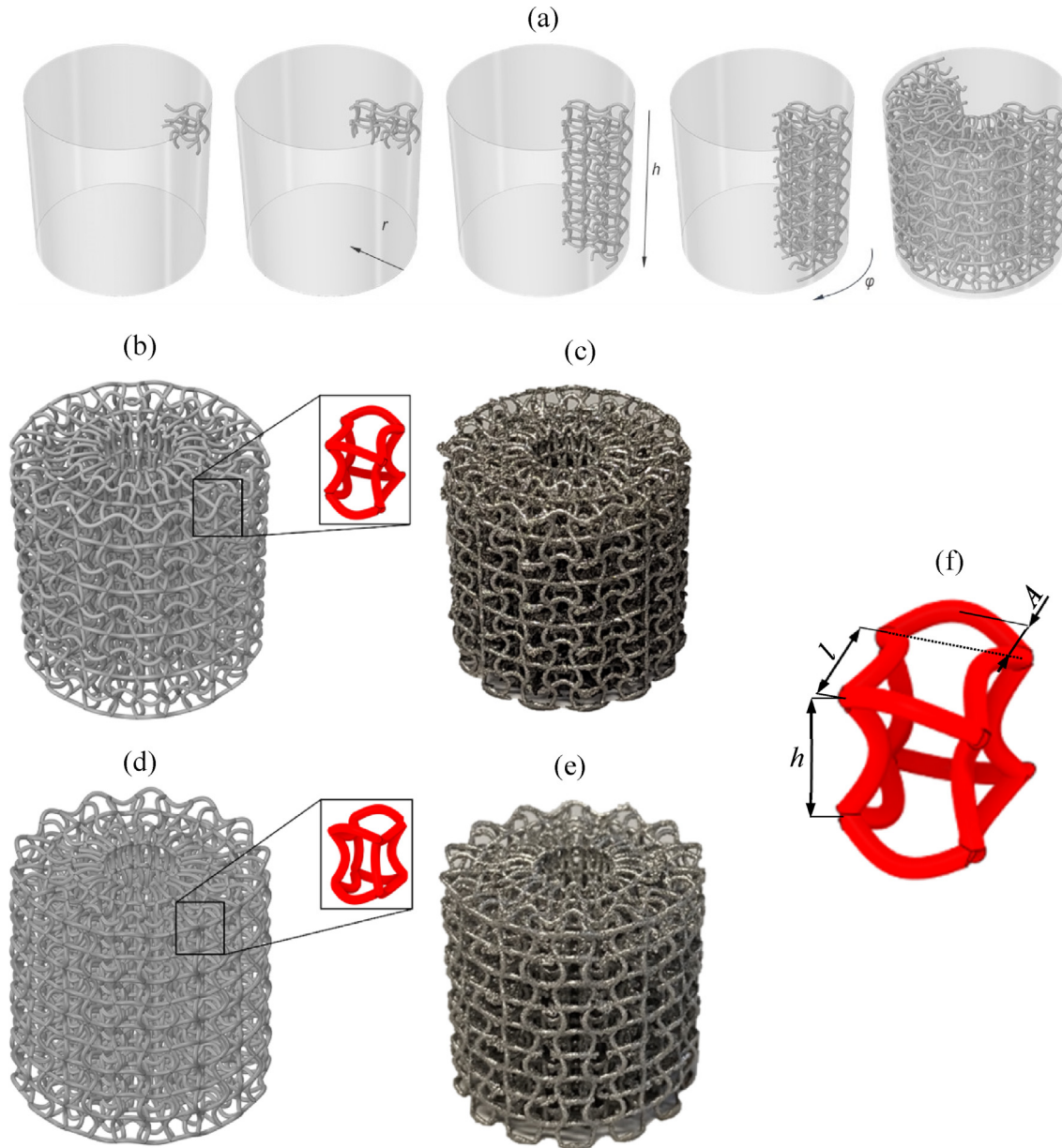
Fig. 1 − **The generation of the axisymmetric chiral structure (a), architected virtual (b,d), fabricated geometry (c,e) of the ACS_v1 and ACS_v2 structure, and geometry of the unit cell, respectively.**

unit cell are the same for ACS_v1 and ACS_v2 structures and are $l = h = 2$ mm and $A = 0.5$ mm in the most outer layer of unit cells. Different relative densities in ACS_v2 structures are achieved using different strut thicknesses.

Six samples of each generated structure were fabricated using the additive manufacturing machine EOS M280 based on a powder bed fusion system. The machine uses a 400W Ytterbium fiber laser with a beam diameter between 100 μm and 500 μm, and scan speeds up to 7 m/s. Gas atomised stainless steel 316L powder was used to fabricate the plate samples with consistent and repeatable geometry [40]. The fabrication imperfection, surface quality and their influence on the mechanical behaviour were already presented in our previous work for the strut based auxetic structures [41] and TPMS structures [42].

The fabricated sample plates were blasted with high-pressure air to remove the surrounding residual powder. The average mass and corresponding relative density of fabricated samples are given in Table 1.

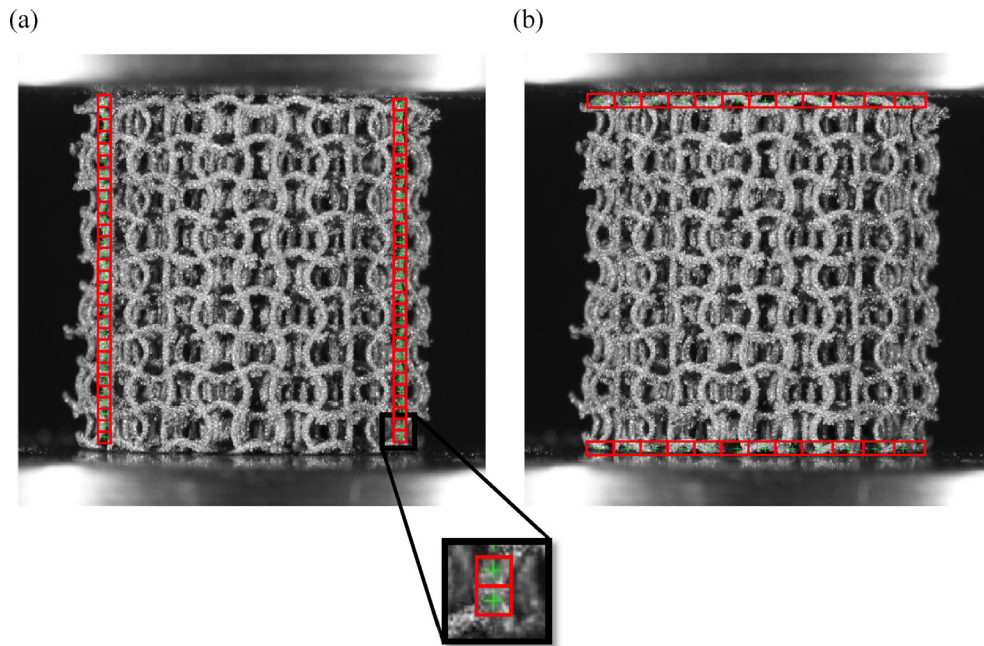| Table 1 − Physical properties of fabricated specimens.			
Geometry	Dimensions [mm]	Weight (st. dev.) [g]	Relative density [%]
ACS_v1	⌀20 × 20	4.37 (0.0.4)	8.5
ACS_v2_relative density6		3.17 (0.11)	5.6
ACS_v2_relative density9		5.21 (0.08)	9.1

Fig. 2 − The vertical (a) and horizontal (b) positioning of DIC correlation points.

3.   Mechanical testing

3.1.   Methods

Uniaxial compression tests following ISO 13314:2011 standard [43] were performed using a servo-hydraulic INSTRON 8801 testing machine with the position-controlled cross-head rate of 0.1 mm/s (quasi-static testing - QS) and 284 mm/s (dynamic testing - DYN) at room temperature of 22 °C. The testing conditions were the same for all analysed specimens. The recorded load-displacement data were converted to engineering stress-strain values, using the initial specimen's dimensions. Macroscopic engineering strain rate was calculated by dividing the loading velocity with the specimen's length in the direction of the loading. The initial engineering strain rates during quasi-static and dynamic testing were 0.005 s^{-1} and 14.2 s^{-1}, respectively. The plateau stress was calculated as average stress in the range of 20−40% compressive strain [43], while the values of specific energy absorption (SEA) were and Crash Force Efficiency (CFE) values were calculated as follows:

$$SEA = \frac{\int_0^{\varepsilon_d} \sigma d\varepsilon}{\rho} \tag{1}$$

$$CFE = \frac{\underset{\varepsilon < \varepsilon_d}{aver\sigma}}{\underset{\varepsilon < \varepsilon_d}{max\sigma}} \times 100\% \tag{2}$$

where ε_d is the densification strain (calculated as strain where the stress reaches 1.3 × plateau stress [44]) and ρ is the density of cellular structure.

The deformation behavior was additionally evaluated using infrared (IR) thermography. IR thermography was applied using high-speed cooled middle-wave IR thermal camera Flir SC 5000 (frame rate 608 Hz with 0.02 K sensitive cooled middle-wave InSb detector) to observe the evolution of plastic deformation of specimens during the dynamic compression testing. This method has already been demonstrated as suitable for deformation pattern recognition and crushing process in various cellular materials subjected to dynamic loading conditions [45,46] and also offers a reliable tool for additional validation of computational models [6].

Digital image correlation (DIC) is a well-known method used for tracking specimen deformation using sequential high-resolution digital imaging. A grid of correlation points needs to be defined at specified image pixels to track the deformation through the sequence of images. In this study, the correlation points were positioned vertically and horizontally on the outer part of the specimen to evaluate longitudinal and transversal strains, respectively. Thirty correlation points were used in the vertical direction and twelve in the horizontal direction. Each point was surrounded by a subset of pixels defining a specific area (Fig. 2). First, the DIC method was used to observe the longitudinal and transversal strains, then used to evaluate the Poisson's ratio. The complete deformation process was captured by an average set of 28 digital images. The image resolution was 1060 px × 1025 px.

3.2.   Results

The mechanical testing results of axisymmetric chiral samples are given in Figs. 3−5, where the single test results are presented with dotted lines, while a solid line represents the average. Figure 3a shows the mechanical response of ACS_v1 samples, where a typical response of cellular materials can be
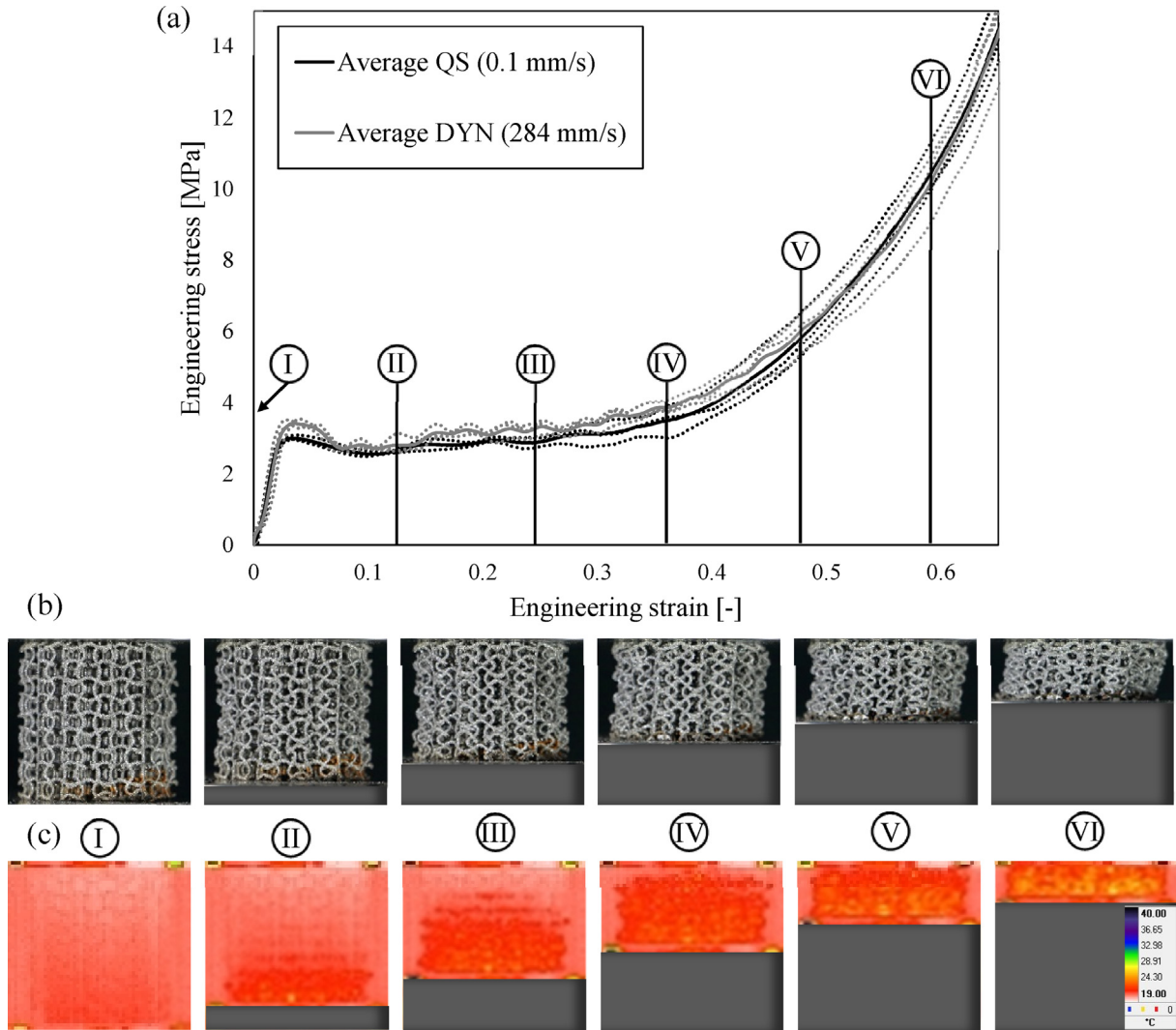
Fig. 3 — The mechanical response (a) and deformation behaviour under quasi-static (b) and dynamic (c) loading conditions of ACS_v1 samples.

observed. The linear elastic region is followed by the plateau region of constant stress, ending in structure densification. The limited strain rate hardening can be observed when comparing the quasi-static and dynamic responses. Figure 3b and c shows the deformation behavior of the samples under the quasi-static loading conditions and dynamic loading conditions using the IR thermography, respectively. The auxetic behavior can be observed in Fig. 3b, further analysed in the section below.

Figure 4a shows the mechanical response of ACS_v2_relative density6 samples. A more pronounced stress drop after the first stress peak can be observed if compared to ACS_v1 samples. The limited strain rate hardening can be again noticed. Figure 4b and c shows the deformation behaviour of the samples under the quasi-static loading conditions and dynamic loading conditions using the IR thermography, respectively. Figure 4b and c shows no apparent auxetic behaviour in ACS_v2_relative density6 samples.

Figure 5a shows the mechanical response of ACS_v2_relative density9 samples. A less pronounced stress drop after the

first stress peak if compared to ACS_v2_relative density6 samples is observed, especially in the case of quasi-static loading. The strain rate hardening is minimal also in this structure. Figure 5b and c shows the deformation behaviour of the samples under the quasi-static loading conditions and dynamic loading conditions using the IR thermography, respectively. Figure 5b and c shows no apparent auxetic behaviour also in ACS_v2_relative density9 samples.

A comparison of the static and dynamic responses of three ACS samples is shown in Fig. 6. The strain rate hardening is observed in all analysed samples and is more pronounced in the samples with higher relative densities.

The deformation behavior was additionally analysed using the DIC, primarily to calculate the Poisson's ratio dependence on the axial strain of specimens, which is illustrated in Fig. 7 for all three tested sample structures. It can be observed that the auxetic effect is less pronounced at higher strains, as it was already observed in previous work [47,48]. However, the Poisson's ratio changes are more gradual in axisymmetric auxetic structures and not abrupt as in regular 3D structures.
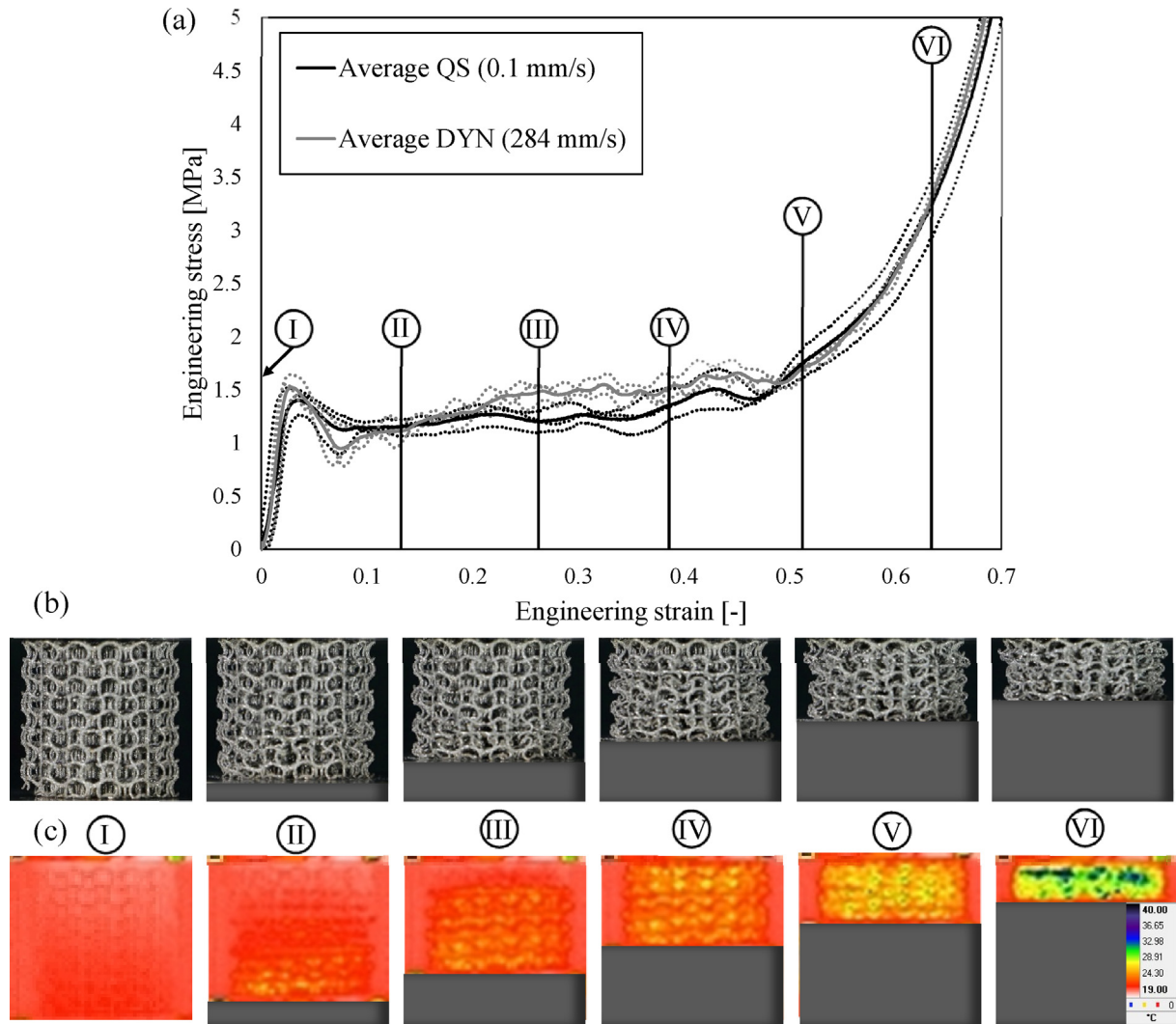
Fig. 4 — The mechanical response (a) and deformation behaviour under quasi-static (b) and dynamic (c) loading conditions of ACS_v2_relative density6 samples.

4. Computational modelling

The finite element software system LS-DYNA [49] was used for all reported computer simulations.

4.1. Material model

The elastoplastic material model (MAT_024) was used to describe the base material's constitutive behaviour of the analysed axisymmetric structures [49]. The model is a rate-dependent, three-piecewise-linear elasto-plastic model with following parameters: density ρ, Young's modulus E, Poisson's ratio ν, initial yield stress σ_{yield}, the definition of linear hardening with the second point in the stress-strain diagram (σ_2, $\varepsilon_{pl,2}$) [50]. Ideal plasticity after the $\varepsilon_{pl,2}$ was assumed to avoid non-physical removal of FE in the case of considered failure. The plastic material parameters were determined by inverse parametric computational simulations of loaded samples to retrieve the same macroscopic simulation results as those

measured in experimental testing for analysed structures and an entire range of strains up to densification. The resulting material parameters of the material model MAT_024 are given in Table 2. The values of yield stresses for AISI 361L are similar to those reported in [51], where the material parameters were determined using different standard tensile and shear specimens.

The top and bottom compression plates were modelled as linear-elastic (material model MAT_ELASTIC) with the following material parameters: density $\rho = 7850$ kg/m^3, Young's modulus $E = 210,000$ MPa and the Poisson's ratio $\nu = 0.3$.

4.2. Boundary conditions and finite element mesh

The generated CAD geometry of samples was transformed to beam finite element mesh, allowing for faster and accurate cellular structure response calculations up to very large deformations. The micro defects in the structure's geometry due to the fabrication procedure were not taken into account
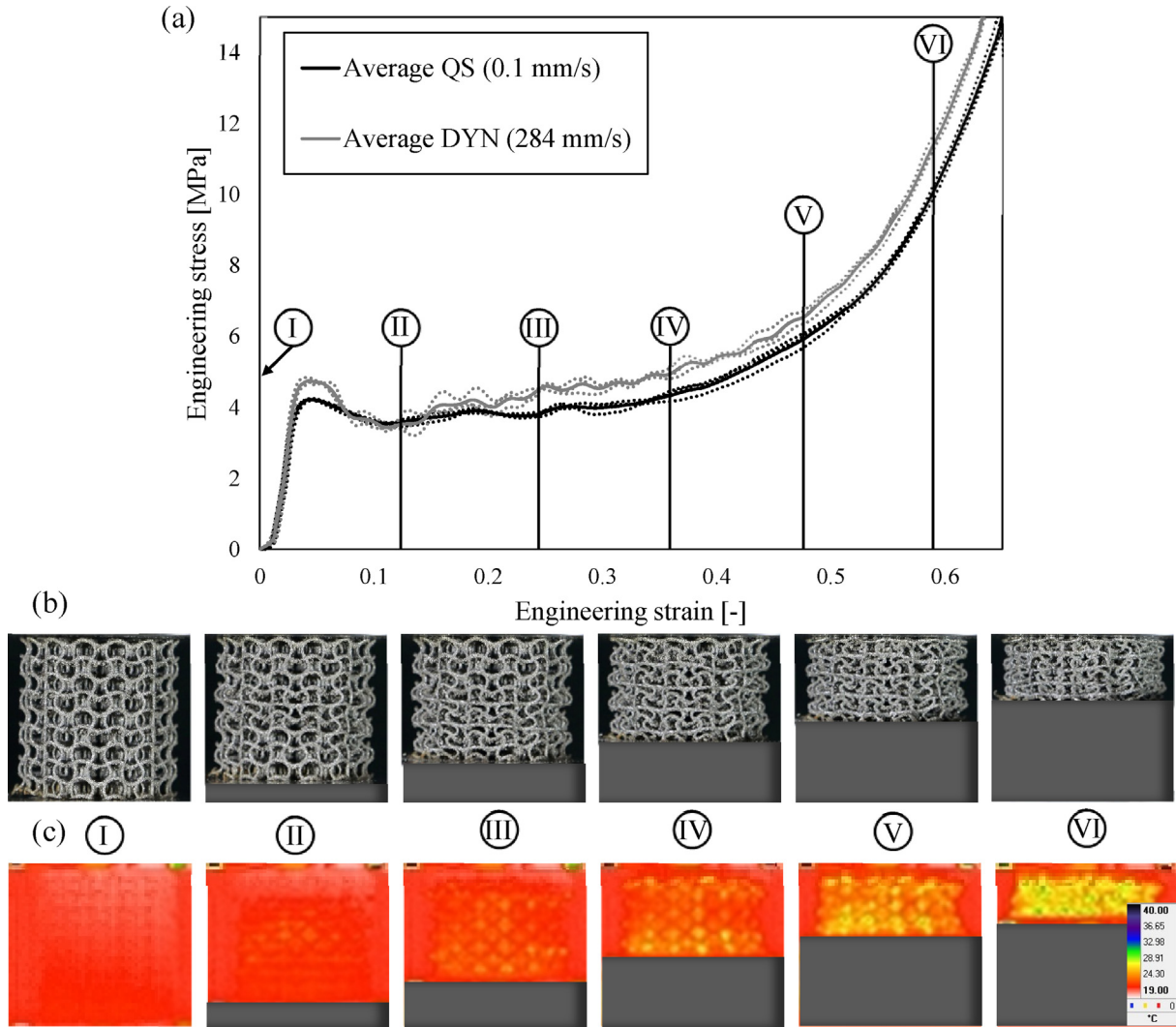
Fig. 5 — The mechanical response (a) and deformation behaviour under quasi-static (b) and dynamic (c) loading conditions of ACS_v2_relative density9 samples.

directly in this type of analysis. Their effect is indirectly considered in the material's constitutive parameters determined by the inverse parametric study. The Hughes-Liu beam finite elements (FE) were used to model the struts of cellular structures, where their circular cross-section was assumed. The average diameter of beam FE in computational models was determined using weight comparison between the CAD model, fabricated specimens (micro-computed tomography), and discretised computational models. The mesh sensitivity analysis was performed with three different FE mesh densities.

The following boundary conditions were used: the bottom compression plate with all degrees of freedom fixed, the top compression plate with prescribed constant velocity (2 m/s)

towards the bottom plate to speed up the computation time (Fig. 8). The scaling of the quasi-static testing velocity (from 0.1 mm/s to 2 m/s) to speed up computations was confirmed as acceptable by parametric computational analysis, where the reaction forces on the bottom and upper plate were compared at different loading velocities.

The node to surface contact formulation with friction was defined between plates and the cellular structure, while the general contact with friction was defined between the beam finite elements of the cellular structure. The coefficient of friction was set to 0.36 and 0.34 for static and dynamic cases [52], respectively. The latter was slightly lower to account for the sliding conditions.

4.3. Results

The deformation behavior of ACS_v1 samples is shown in Fig. 9, where it can be observed that the computed deformation pattern is very similar to the one observed in the experiments (Fig. 3a). As observed in the experiments, the cells on the outer

Table 2 — The MAT_024 material model parameters.

| ρ [kg/m³]	E [MPa]	ν [-]	σ_{yield} [MPa]	σ_2 [MPa]	$\varepsilon_{pl,2}$ [-]
7850	210,000	0.3	450	650	0.3
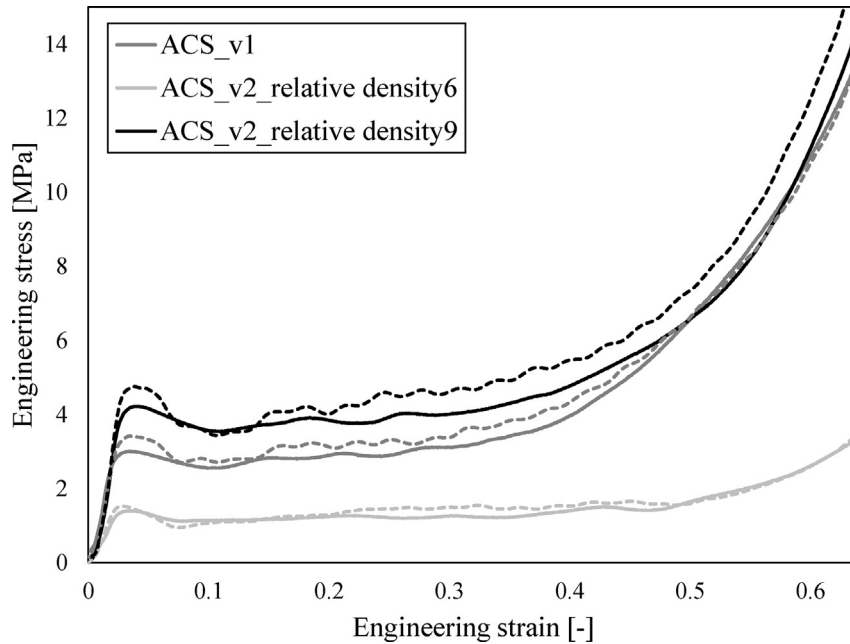
Fig. 6 − The average mechanical responses of ACS structures under quasi-static (solid lines) and dynamic (dashed lines) loading conditions.

structure part are not extensively deformed compared to the cells on the inner part of the structure. The computational modeling offers a possibility to easily track the deformation process on the inside of the samples. This is very relevant in the studied cases where localisation results from the cell geometry, which is narrower in the structure's inner part.

The comparison of the mechanical responses between the experimental and computational results is shown in Fig. 10. Excellent agreement between the results can be observed for the ACS_v1 and ACS_v2_relative density9 samples. The computational model overestimated the response in the

ACS_v2_relative density6 structure due to increased fabrication imperfection influence at the low relative density samples, as already observed in our previous work [6]. The developed computational model very well captures the overall mechanical response of all analysed geometries.

The Poisson's ratio in the FE model was determined with the same methodology used in the experiments (DIC correlation) by measuring nodal displacements at the same correlation points. Figure 7 shows a good correlation between the experimental and FE results in the entire analysed strain range. The Poisson's ratio strain dependency observed in
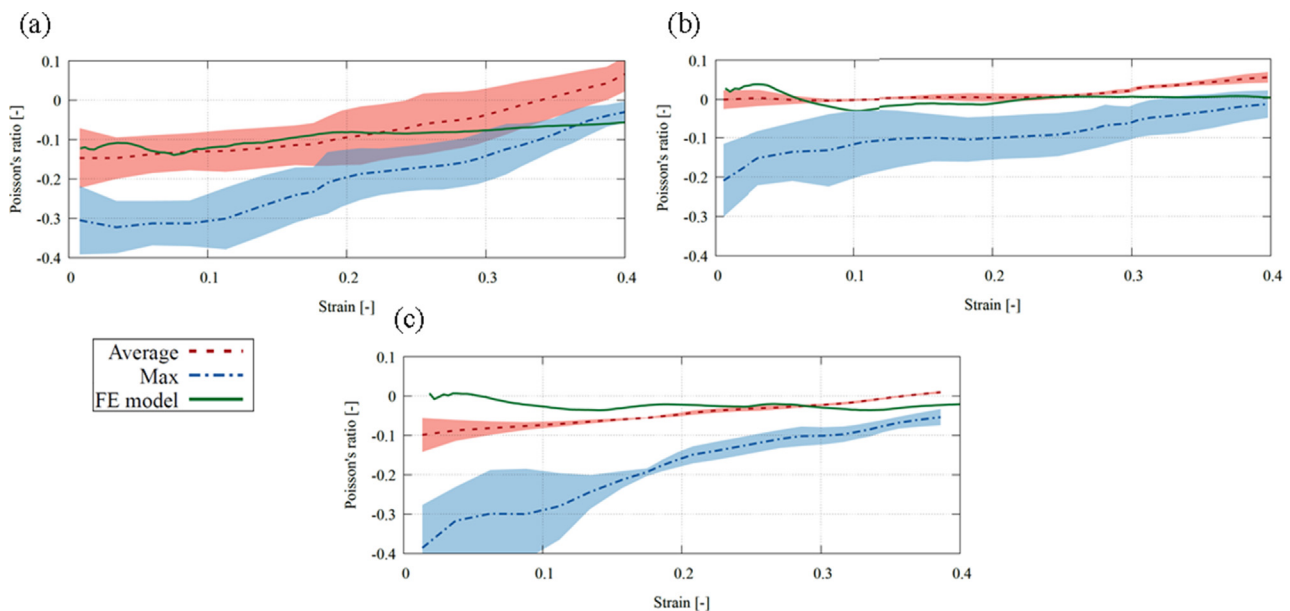
Fig. 7 − The Poisson's ratio's strain dependence in the experiment and FE model (a) ACS_v1, (b) ACS_v2_relative density6 and (c) ACS_v2_relative density9.
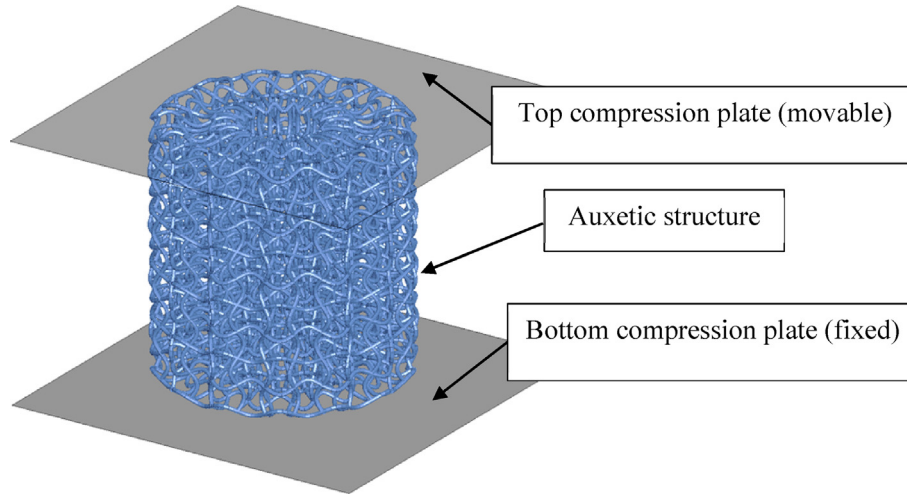
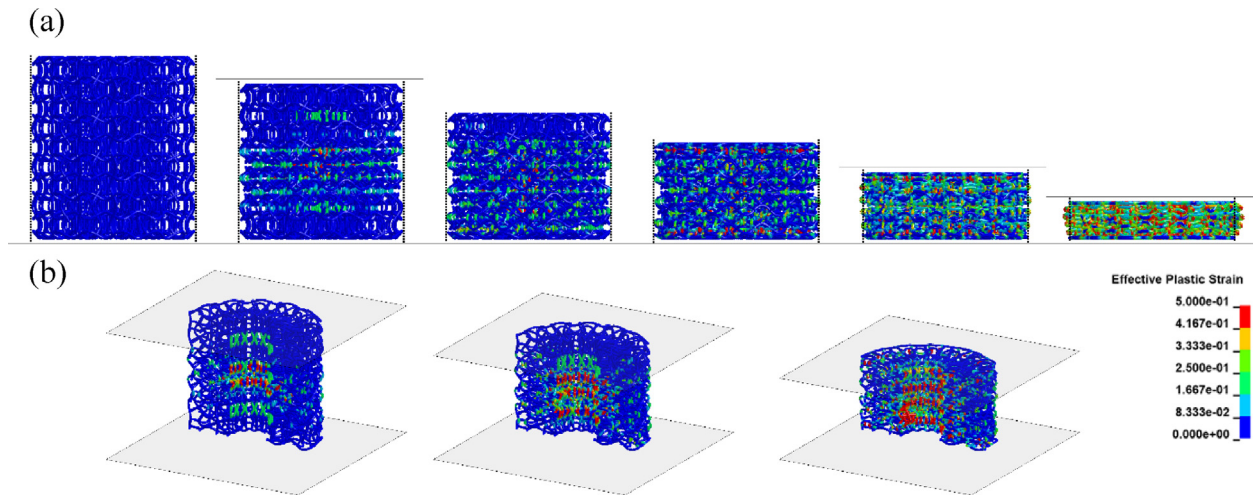Fig. 8 – Computational model of the axisymmetric auxetic structure.

Fig. 9 – The deformation analysis of ACS_v1 FE model (a), and deformation localisation analysis (b) (strain increment: 15%).

Table 3 – Graded axisymmetric chiral structure data.						
Geometry	Dimensions [mm]	t_1 [mm]	t_2 [mm]	t_3 [mm]	Weight [g]	Relative density [%]
Uniform (ACS_v1)	$\varnothing 20 \times 20$	0.34	0.34	0.34	4.37	8.5
Graded v1		0.24	0.29	0.34	3.55	6.9
Graded v2		0.20	0.25	0.34	3.20	6.2
Graded v3		0.20	0.30	0.40	4.38	8.5
Graded v4		0.30	0.40	0.50	7.29	14.2

computational simulations is less pronounced, with Poisson's ratio almost constant up to 40% strain in all analysed cases. This is a consequence of an ideal geometry used in the computational models resulting in a uniform and homogeneous deformation in contrast to observed localised deformation in actual samples due to local fabrication defects.

The parametric computational study of axisymmetric chiral structure with simply graded porosity was performed next. The base geometry of the uniform v1 structure was divided into three concentric rings (Fig. 12) with varying strut thicknesses (t_1, t_2 and t_3) per ring assigned, as given in Table 3.

The deformation behavior of the graded axisymmetric chiral structure v3 is shown in Fig. 11. This structure was chosen as an example since it has the same relative density as the uniform structure v1 (original design in Table 1). By comparing the deformation behavior in Fig. 11 (graded structure) and Fig. 9 (uniform structure), one can observe less localised deformation in the central ring in the former structure. This contributes to graded structures' more predictable mechanical response (Fig. 12), with a smaller stress drop after the initial peak. The peak stress, stress plateau and densification strain again clearly show a dependence of the relative density.
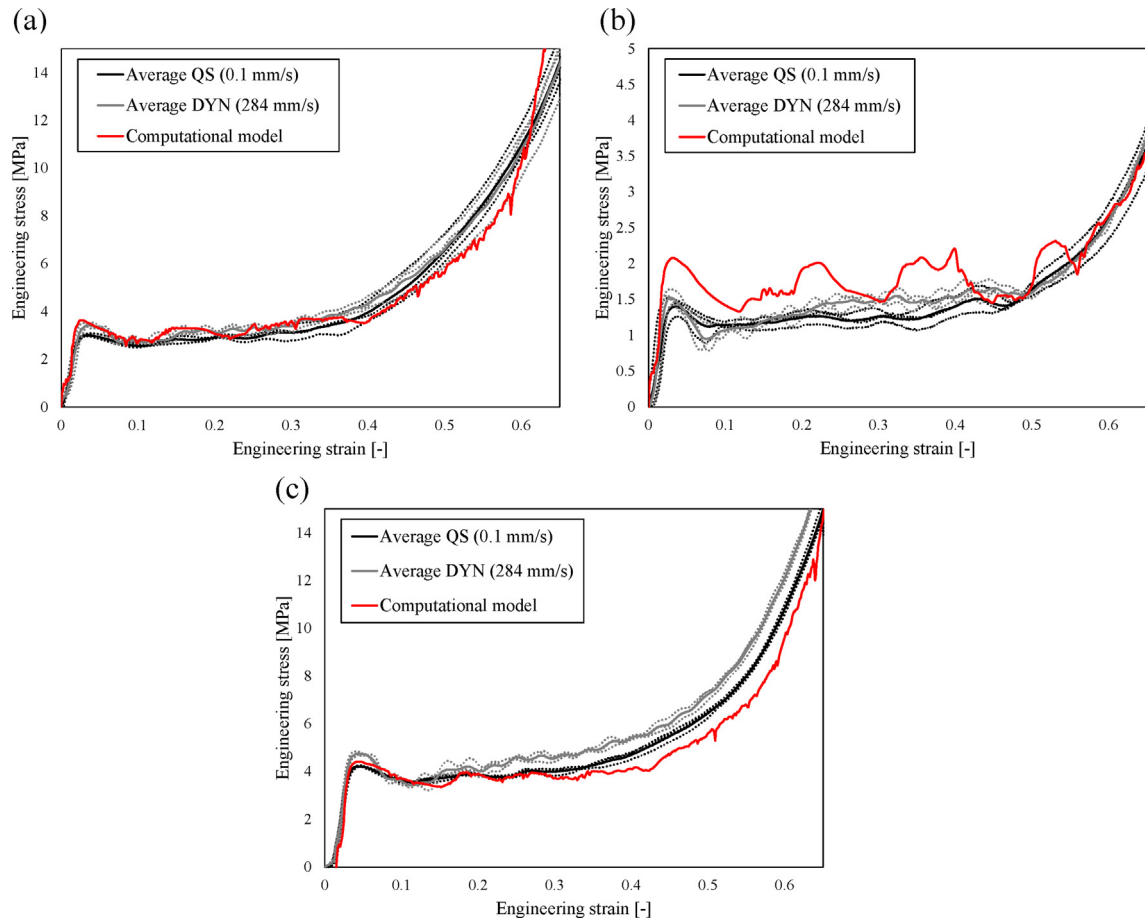
Fig. 10 — Comparison of experimental and computational results for ACS_v1 (a), ACS_v2_relative density6 (b) and ACS_v2_relative density9 (c) samples.

5. Results analysis

The peak force and calculated SEA results are given in Table 4 and compared to the previous work. As expected, the plateau and peak stresses are higher in structures with higher relative densities. The SEA increases with relative density increase since the fabrication defects caused by additive manufacturing have a minor effect in structures with higher relative densities.

Compared to the previously published data on the behaviour of chiral structures, the SEA is comparable to structures made of titanium [31] and much higher than in structures made of copper [38].
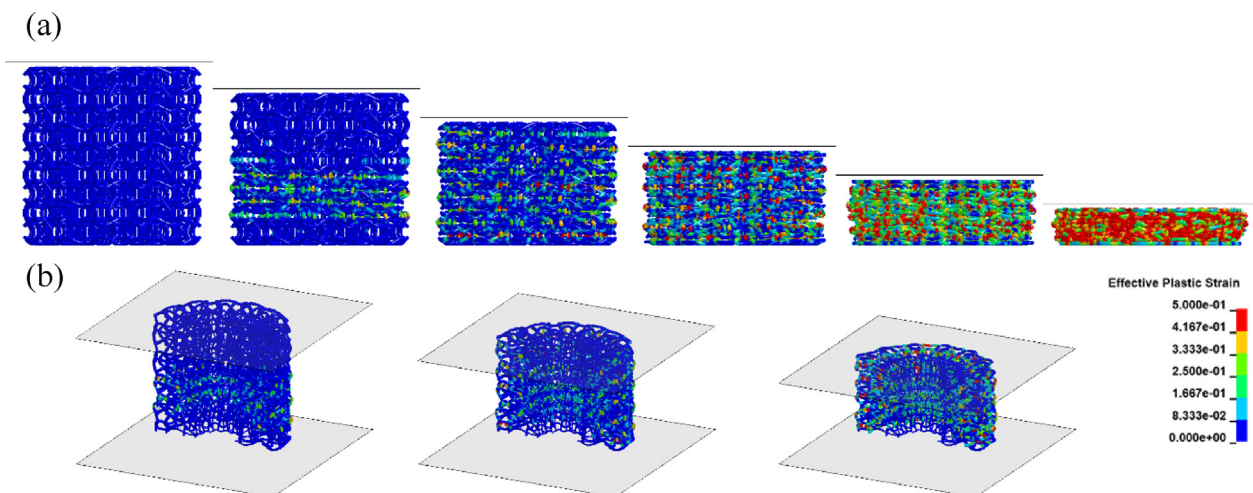
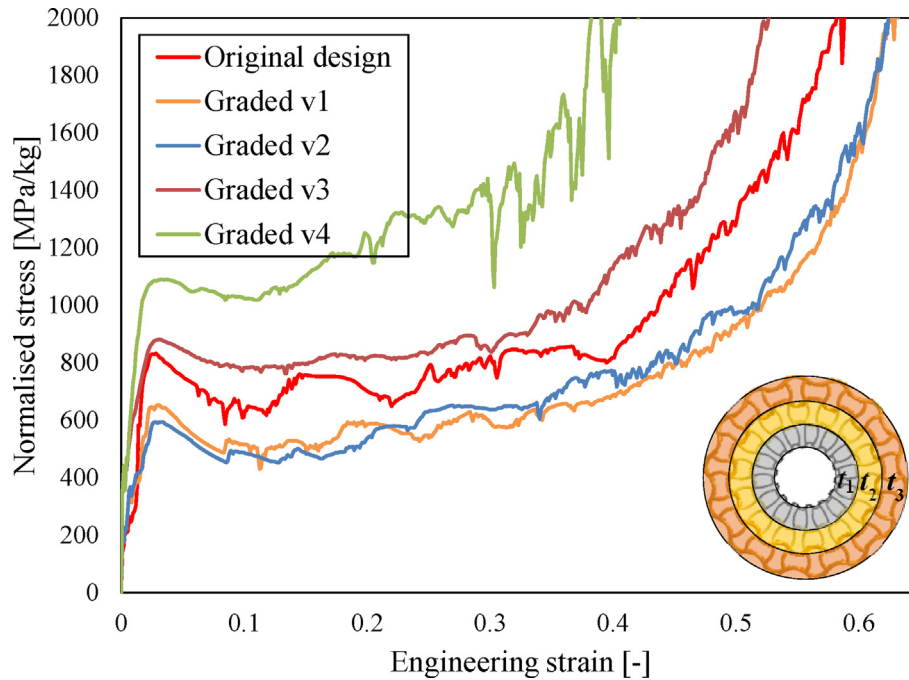**Fig. 11 — Deformation behaviour of v3 graded structure.**

Fig. 12 — Mechanical responses of graded axisymmetric chiral structures.

Table 4 — Peak force and SEA analysis of different auxetic structures.

Sample	relative density [%]	Plateau stress [MPa]		Peak stress [MPa]		SEA to 40% [J/g]	
		QS	DYN	QS	DYN	QS	DYN
ACS_v1	8.5	3.21	3.54	3.00	3.42	1.73	1.89
ACS_v1 − computational		3.43		3.64		1.91	
ACS_v2_relative density6	5.6	1.24	1.45	1.40	1.52	1.05	1.13
ACS_v2_relative density6 − comptutational		1.82		2.08		1.55	
ACS_v2_relative density9	9.1	4.04	4.60	4.23	4.76	2.00	2.20
ACS_v2_relative density9 − comptutational		3.85		4.41		2.03	
Chiral Ti [37]	4.1	0.67	0.70	1.03	1.08	1.78	1.79
Chiral Copper [38]	7.2	0.32	0.33	0.40	0.41	0.21	0.22

Table 5 — Densification strain and CFE of analysed cellular structures.

Sample	Densification strain [%]		CFE [%]	
	QS	DYN	QS	DYN
ACS_v1	41	42	70.83	67.99
ACS_v2_relative density6	49	54	80.00	65.80
ACS_v2_relative density9	48	44	66.92	72.79

The results showed no influence of the negative Poisson's ratio in structure v1 compared to v2 structure. For that reason, the subsequent computational study was conducted for the v1 structure with the relative density of 9.1%, which returned the plateau stress of 4.9 MPa, peak stress 4.88 MPa and SEA 2.60 J/g, making this structure superior when compared to the v2 structure.

In order to evaluate the energy absorption efficiency of the newly developed cellular structures, the densification strain and Crash Force Efficiency (CFE) values were also calculated (Table 5). As can be seen from Table 5, the structure with lowest relative density offers highest CFE among the analyses cellular structures, while the ACS_v1 sample provides the most constant CFE value when the loading velocity is changed.

6.   Conclusions

Novel axisymmetric chiral structures (CAS) were developed to obtain new tubular structures with a negative Poisson's ratio. The structures were developed using the computed aided design and manufactured using additive manufacturing technologies. Two different geometries with different relative densities were analysed. The energy absorption analysis reveals better mechanical properties of axisymmetric structures compared to conventional (orthogonal) counterparts.

The experimental results validate the newly developed computational model, which returns comparable deformation

behavior and Poisson's ratio. The validated computational models help develop new geometries and study their behavior under different loading conditions virtually. The validated computational model was used to evaluate the performance of a simple axisymmetric chiral structure with graded porosity. The new structure shows a more uniform stress distribution and therefore results in higher energy absorption capabilities.

The optimisation algorithms used to design graded CAS with tailored mechanical properties and uniform stress distribution are envisaged in the following studies, leading to improved applicability of these structures in engineering, medicine, and sports.

Data availability

The data that support the findings of this study are available on request from the corresponding author.

Declaration of Competing Interest

The authors declare that they have no known competing financial interests or personal relationships that could have appeared to influence the work reported in this paper.

Acknowledgments

REFERENCES

[1] Evans KE, Caddock BD. Microporous materials with negative Poisson's ratios. II. Mechanisms and interpretation. J Phys D Appl Phys 1989;22:1883—7.

[2] Novak N, Vesenjak M, Ren Z. Auxetic cellular materials - a Review. Strojniški Vestn. - J. Mech. Eng. 2016;62(9):485—93.

[3] Airoldi A, Novak N, Sgobba F, Gilardelli A, Borovinšek M. Foam-filled energy absorbers with auxetic behaviour for localised impacts. Mater Sci Eng,A 2020;788.

[4] Mauko A, Fíla T, Falta J, Koudelka P, Rada V, Neuhäuserová M, et al. Dynamic deformation behaviour of chiral auxetic lattices at low and high strain-rates. Metals (Basel) 2021;11:1.

[5] Schwerdtfeger J, Schury F, Stingl M, Wein F, Singer RF, Körner C. Mechanical characterisation of a periodic auxetic structure produced by SEBM. Phys Status Solidi 2012;249(7):1347—52.

[6] Novak N, Vesenjak M, Krstulović-Opara L, Ren Z. Mechanical characterisation of auxetic cellular structures built from inverted tetrapods. Compos Struct 2018;196:96—107.

[7] Assidi M, Ganghoffer J-F. Composites with auxetic inclusions showing both an auxetic behaviour and enhancement of their mechanical properties. Compos Struct Jul. 2012;94(8):2373—82.

[8] Ghazlan A, Ngo T, Tan P, Xie YM, Tran P, Donough M. Inspiration from Nature's body armours — a review of biological and bioinspired composites. Composites Part B Eng 2020;205:108513.

[9] Liu Z, Meyers MA, Zhang Z, Ritchie RO. Functional gradients and heterogeneities in biological materials: design principles, functions, and bioinspired applications. Prog Mater Sci 2017;88:467—98.

[10] Fang Y, Wang Y, Hou C, Lu B. CFDST stub columns with galvanised corrugated steel tubes: concept and axial behaviour. Thin-Walled Struct Dec. 2020;157:107116.

[11] Tarlochan F, Samer F, Hamouda AMS, Ramesh S, Khalid K. Design of thin wall structures for energy absorption applications: enhancement of crashworthiness due to axial and oblique impact forces. Thin-Walled Struct Oct. 2013;71:7—17.

[12] Yuan L, Shi H, Ma J, You Z. Quasi-static impact of origami crash boxes with various profiles. Thin-Walled Struct Aug. 2019;141:435—46.

[13] Zahran MS, Xue P, Esa MS, Abdelwahab MM. A novel tailor-made technique for enhancing the crashworthiness by multi-stage tubular square tubes. Thin-Walled Struct Jan. 2018;122:64—82.

[14] Feng R, Wu C, Chen Z, Roy K, Chen B, Lim JBP. An experimental study on stainless steel hybrid tubular joints with square braces and circular chord. Thin-Walled Struct Oct. 2020;155:106919.

[15] Feng R, Huang Z, Chen Z, Roy K, Chen B, Lim JBP. Finite-element analysis and design of stainless-steel CHS-to-SHS hybrid tubular joints under axial compression. Thin-Walled Struct Jun. 2020;151:106728.

[16] Ling B, Wei K, Qu Z, Fang D. Design and analysis for large magnitudes of programmable Poisson's ratio in a series of lightweight cylindrical metastructures. Int J Mech Sci Apr. 2021;195:106220.

[17] Khurram Wadee M, Ahmer Wadee M, Bassom AP. Effects of orthotropy and variation of Poisson's ratio on the behaviour of tubes in pure flexure. J Mech Phys Solid 2007;55(5):1086—102.

[18] Cao X, Huang Z, He C, Wu W, Xi L, Li Y, et al. In-situ synchrotron X-ray tomography investigation of the imperfect smooth- shell cylinder structure,. Compos Struct 2021. https://doi.org/10.1016/j.compstruct.2021.113926.

[19] Luo C, Han CZ, Zhang XY, Zhang XG, Ren X, Xie YM. Design, manufacturing and applications of auxetic tubular structures: a review. Thin-Walled Struct Jun. 2021;163:107682.

[20] Scarpa F, Smith CW, Ruzzene M, Wadee MK. Mechanical properties of auxetic tubular truss-like structures. Phys. Status Solidi Basic Res. 2008;245(3):584—90.

[21] Gatt R, Caruana-Gauci R, Attard D, Casha AR, Wolak W, Dudek K, et al. On the properties of real finite-sized planar and tubular stent-like auxetic structures. Phys. Status Solidi Basic Res. 2014;251:321.

[22] Wu W, Tao Y, Xia Y, Chen J, Lei H, Sun L, et al. Mechanical properties of hierarchical anti-tetrachiral metastructures. Extrem. Mech. Lett. 2017;16:18.

[23] Hamzehei R, Rezaei S, Kadkhodapour J, Anaraki AP, Mahmoudi A. 2D triangular anti-trichiral structures and auxetic stents with symmetric shrinkage behavior and high energy absorption. Mech Mater Mar. 2020;142:103291.

[24] Guo C, Zhao D, Liu Z, Ding Q, Gao H, Yan Q, et al. The 3D-printed honeycomb metamaterials tubes with tunable negative Poisson's ratio for high-performance static and

dynamic mechanical properties. Materials (Basel) 2021;14. https://doi.org/10.3390/ma14061353.

[25] Ren X, Liu FC, Zhang XY, Xie YM. Numerical investigation of tubular structures generated by cutting method and pattern scale factor (PSF) method. Pigment Resin Technol 2019;50(5):419–25.

[26] Ren X, Shen J, Tran P, Ngo TD, Xie YM. Auxetic nail: design and experimental study. Compos Struct 2017;184(October):288–98.

[27] Gao Q, Zhao X, Wang C, Wang L, Ma Z. Multi-objective crashworthiness optimisation for an auxetic cylindrical structure under axial impact loading. Mater Des Apr. 2018;143:120–30.

[28] Nejad AF, Alipour R, Rad MS, Yahya MY, Koloor SSR, Petrů M. Using finite element approach for crashworthiness assessment of a polymeric auxetic structure subjected to the axial loading. Polymers 2020;12(6).

[29] Yu X, Yuan X, Ren X, Min Y, Wu Y, Yi Y. A novel type of tubular structure with auxeticity both in radial direction and wall thickness. Thin-Walled Struct 2021;163(March):107758.

[30] Vesenjak M, Duarte I, Baumeister J, Göhler H, Krstulović-Opara L, Ren Z. Bending performance evaluation of aluminium alloy tubes filled with different cellular metal cores. Compos Struct Feb. 2020;234:111748.

[31] Gao Q, Liao W-H, Wang L, Huang C. Crashworthiness optimisation of cylindrical negative Poisson's ratio structures with inner liner tubes. Struct Multidiscip Optim 2021;64(6):4271–86.

[32] Körner C, Liebold-Ribeiro Y. A systematic approach to identify cellular auxetic materials. Smart Mater Struct 2014;24. 025013.

[33] Warmuth F, Körner C. Phononic band gaps in 2D quadratic and 3D cubic cellular structures. Materials 2015;8(12):8327–37.

[34] Wormser M, Warmuth F, Körner C. Evolution of full phononic band gaps in periodic cellular structures. Appl Phys A 2017;123(661).

[35] Warmuth F, Osmanlic F, Adler L. Fabrication and characterisation of a fully auxetic 3D lattice structure via selective electron beam melting. Smart Mater Struct 2017;26:8.

[36] Vesenjak M, Novak N, Ren Z. Axisymmetric chiral auxetic structure, EP21197296.3 patent pending. 2021.

[37] Novak N, Starčevič L, Vesenjak M, Ren Z. Blast response study of the sandwich composite panels with 3D chiral auxetic core. Compos Struct 2019;210:167–78.

[38] Novak N, Vesenjak M, Tanaka S, Hokamoto K, Ren Z. Compressive behaviour of chiral auxetic cellular structures at different strain rates. Int J Impact Eng Jul. 2020;141:103566.

[39] Novak N, Krstulović-Opara L, Ren Z, Vesenjak M. Compression and shear behaviour of graded chiral auxetic structures. Mech Mater 2020;148. https://doi.org/10.1016/j.mechmat.2020.103524.

[40] Novak N, Al-ketan O, Krstulović-Opara L, Rowshan R, Al-rub RKA, Vesenjak M, et al. Quasi-static and dynamic compressive behaviour of sheet TPMS cellular. Compos Struct 2021;266:113801.

[41] Novak N, Borovinšek M, Vesenjak M, Wormser M, Körner C, Tanaka S, et al. Crushing behavior of graded auxetic structures built from inverted tetrapods under impact. Phys Status Solidi B 2018;256:1.

[42] Novak N, Al-Ketan O, Borovinšek M, Krstulović-Opara L, Rowshan R, Vesenjak M, et al. Development of novel hybrid TPMS cellular lattices and their mechanical characterisation. J Mater Res Technol 2021;15:1318–29. https://doi.org/10.1016/j.jmrt.2021.08.092.

[43] ISO 13314:2011. Mechanical testing of metals - ductility testing - compression test for porous and cellular metals. Geneva, Switzerland: International Organization for Standardization; 2011.

[44] Hipke T, Lange G, Poss R. Taschenbuch für Aluminiumschäume. Düsseldorf: Alu Media; 2007.

[45] Duarte I, Vesenjak M, Krstulović-Opara L, Ren Z. Static and dynamic axial crush performance of in-situ foam-filled tubes. Compos Struct 2015;124:128–39.

[46] Vesenjak M, Gačnik F, Krstulović-Opara L, Ren Z. Mechanical properties of advanced pore morphology foam elements. Mech Adv Mater Struct 2015;22(5):359–66.

[47] Novak N, Dobnik Dubrovski P, Borovinšek M, Vesenjak M, Ren Z. Deformation behaviour of advanced textile composites with auxetic structure. Compos Struct 2020;252:112761.

[48] Novak N, Duncan O, Allen T, Alderson A, Vesenjak M, Ren Z. Shear modulus of conventional and auxetic open-cell foam. Mech Mater 2021;157:103818.

[49] Hallquist J. LS-DYNA keyword user's manual. Livermore, California: Livermore Software Technology Corporation; 2007.

[50] Marzi S, Hesebeck O, Brede M, Kleiner F. A rate-dependent, elasto-plastic cohesive zone mixed-mode model for crash analysis of adhesively bonded joints. In: 7th European LS-DYNA conference; 2009.

[51] Li X, Roth CC, Tancogne-dejean T, Mohr D. Rate- and temperature-dependent plasticity of additively manufactured stainless steel 316L: characterisation, modeling and application to crushing of shell-lattices. Int J Impact Eng 2020:103671.

[52] Blau PJ. Friction science and technology. CRC Press; 2008.